Scattering by whistler-mode waves during a quiet period perturbed by substorm activity

Jean-François Ripoll, Mick H. Denton, David P. Hartley, Geoffrey D. Reeves, David Malaspina, Gregory S. Cunningham, Ondrej Santolík, Scott A. Thaller, Vivien Loridan, J.F. Fennell, et al.

Scattering by whistler-mode waves during a quiet period perturbed by substorm activity

J.-F. Ripoll
CEA, DAM, DIF, F-91297 Arpajon, France
UPS, CEA, LMCE, 91680 Bruyères-le-Châtel, France

M. H. Denton,
New Mexico Consortium, Los Alamos, NM 87544, USA
Space Science Institute, Boulder, CO 80301, USA.

D. P. Hartley
Department of Physics and Astronomy, University of Iowa, Iowa City, Iowa, USA

G. D. Reeves
Los Alamos National Laboratory, Los Alamos, New Mexico, USA
New Mexico Consortium, Los Alamos, NM 87544, USA

D. Malaspina
Department of Astrophysical and Planetary Sciences, University of Colorado, Boulder, CO, USA
Laboratory for Atmospheric and Space Physics, University of Colorado, Boulder, CO, USA

G. S. Cunningham,
Los Alamos National Laboratory, Los Alamos, New Mexico, USA

O. Santolík
Faculty of Mathematics and Physics, Charles University, Prague, Czech Republic
Department of Space Physics, Institute of Atmospheric Physics, The Czech Academy of Sciences, Prague, Czech Republic

S. A. Thaller
Laboratory for Atmospheric and Space Physics, University of Colorado, Boulder, CO, USA

V. Loridan
ONERA, FR-91123 Palaiseau, France

J. F. Fennell, D. L. Turner
Space Sciences Department, The Aerospace Corporation, El Segundo, California, USA

W. S. Kurth, C. A. Kletzing
Department of Physics and Astronomy, University of Iowa, Iowa City, Iowa, USA

M. G. Henderson,
Los Alamos National Laboratory, Los Alamos, New Mexico, USA

A. Y. Ukhorskiy
Applied Physics Laboratory, Johns Hopkins University, Laurel, Maryland, USA.

Corresponding author: J.-F. Ripoll, CEA, DAM, DIF, F-91297 Arpajon, France (jean-francois.ripoll@cea.fr)

Abstract (150):

We study the dynamics of radiation belt electrons during a 10-day quiet period perturbed by substorm activity and preceding a high-speed stream (HSS), aiming at a global description of the radiation belts in L-shell, L in [2, 6], and energy [0.1, 10] MeV. We combine Van Allen Probes observations and Fokker-Planck numerical simulations of pitch-angle diffusion. The Fokker-Planck model uses event-driven pitch angle diffusion coefficients from whistler-mode waves, built from the wave properties and the ambient plasma density measurements from the Van Allen Probes. We first find this event has some similar characteristics to regular quiet times previously studied; a widely extended plasmasphere within which we observe strong and varying whistler-mode waves. These ambient conditions lead to strong pitch-angle scattering, which contributes to the creation of a wide slot region as well as a significant decay of the outer radiation belts, which are observed and qualitatively well simulated. In addition, we find the substorm activity causes short duration (within +/- 4h) decay of the plasma density and a lowering amplitude of the whistler-mode waves within the plasmasphere, both causing opposite effects in terms of pitch angle diffusion. This leads to a diminution of pitch-angle diffusion at the time of the main substorm activity. Conversely, whistler-mode waves become enhanced in the time periods between the substorm injections. All effects cumulated, we find an enhancement of pitch angle diffusion by whistler-mode waves above L~4.7 during the 10-day period. This directly relates to the combination of quietness and substorm activity which allows pitch angle diffusing of up to 1 MeV electrons in the outer belt. Relativistic electrons of 1 to 2 MeV remain trapped in the

outer belt, from L~4.7 to L~5.2, forming, in both the observations and the simulations, a distinct pocket of remnant electrons.

Keywords:

Electron, wave-particle interactions, radiation belts, moderate substorm activity, substorm, whistler waves.

1. Introduction

Earth's electron radiation belts consist of two toroidal belts of energetic charged particles (~0.1 to ~10 MeV) surrounding Earth, with the inner belt sitting between 1 and 3 Earth radii (R_E) and the outer belt typically lying between 3 and 7 R_E in the equatorial plane. Between the two radiation belts lies a zone often devoid of electrons, called the slot region. This ideal representation is highly dynamic in both space and time; first, because dynamic/disturbed conditions bring complex dynamic mono- (e.g. Reeves et al., 2013) or multi-belt structures (e.g., Baker et al., 2013) and, second, because Earth's radiation belt location is energy dependent (e.g. Lyons and Thorne, 1973). In this work, we specifically address the energy dependence of the radiation belts, between 2 and 6 R_E in the equatorial plane, during a period of quiet state perturbed by substorm activity (e.g. Friedel et al., 1996; Turner et al., 2015) and preceding a high-speed solar wind-stream (HSS) (Denton et al., 2017). We focus on the characterization of the fast slot formation and the outer belt decay, which leads to a drastic reduction in the flux level of the whole radiation belt system (e.g. Reeves et al., 2016; Ripoll et al., 2016a). Understanding the variability of the electron radiation belts, to the point of predictability, is one of the great outstanding challenges in space weather research (cf. review in Ripoll et al.. (2020) and references therein). All progress made will converge toward new advances in the hardening of electronic spacecraft systems and their protection from severe space weather conditions.

This study is based on the analysis of high-quality electron flux observations from NASA's Van Allen Probes (Mauk et al., 2013). Data analysis is supported by computations made with the CEVA code (e.g. Reveillé et al., 2002) that is based on the quasi-linear Fokker-Planck formalism. We feed the CEVA code with event-specific pitch-

angle diffusion coefficients (Ripoll et al., 2016a, 2017, 2019a, 2019b) that are computed from in-situ measurements of plasmaspheric hiss waves and the plasma density observations made by the Van Allen Probes. This computational step requires massivelly parallel computations in order to perform the computation of diffusion coefficients at each satellite outbound pass at time, t, and location, L, i.e. $D_{\alpha 0 \alpha 0}(w_i(t,L), n_e(t,L), E, \alpha_0)$, knowing the various locally measured wave properties, generically denoted here $w_i(t,L)$ for i=1…4, and the plasma density, $n_e(t,L)$, for any electron of energy, E, and equatorial pitch angle, α_0. An alternative methodology is the computation of a single diffusion coefficient from statistical mean properties, $D_{\alpha 0 \alpha 0}(\widehat{w_i}, \widehat{n_e}, L, E, \alpha_0)$ (with $\widehat{(.)}$ denoting a temporal average) which has low numerical cost but neglects correlations between the properties of the ambient domain and, therefore, introduces some error. This method is applied, for instance, to study hiss waves effects in Ma et al. (2016). Our effort of keeping the plasma/wave coupling is motivated by the will to reach the maximum accuracy possible, though approximations always remain (cf. discussion in section 4). This event-driven method has proven successful for an event of 10 days during a quiet period of March 2013 (Ripoll et al., 2016a, 2017, 2019a, 2019b). The new questions we address herein are: can this event-driven method be successful when applied to another, more complex and dynamic, event? How does substorm activity affect the results, their accuracy, and the method?

Section 2 of the article describes the event chosen for this study, including the presentation of both the whistler-mode waves and the plasmasphere activity. In Section 3 we discuss the numerical method used to compute the event-specific pitch-angle diffusion coefficients. Section 4 shows and discusses NASA's Van Allen Probes flux observations and the quasi-linear simulations of the scattering associated to the whistler-mode wave activity that sustains our analysis. We explain that the moderate

substorm activity contributes to decreasing plasmaspheric density, which, in turn, enhances pitch angle diffusion from whistler-mode waves. However, this effect is found insufficient to compensate for the lowering of whistler-mode wave amplitudes that occurs simultaneously. There is nevertheless an enhancement of the mean scattering above L~4.7 for electrons up to 1 MeV. This is attributed to the strengthening hiss activity which occurs in between the substorm injections.

2. Case analysis: 30 of June 2014 – 10 of July 2014

In this study, we examine the evolution of the radiation belts during a 10-day period in 2014, from 30 June to 10 July. This period corresponds to a period of *calm-to-storm* geomagnetic conditions, for which the upcoming storm at the end of the event is driven by high-speed solar wind-streams (HSSs). This event was selected in Denton et al. (2017) who studied the evolution of the ions composition during a 10 day interval preceding the HSS and the HSS itself. High-speed solar wind-streams are well described in Borovsky & Denton (2009, 2010, 2016), Denton & Borovsky (2012, 2017) and Denton et al. (2016) and Hartley et al., 2013 and references therein. This type of event leads to the injection of fresh plasma into the inner magnetosphere, via geosynchronous orbit (GEO), (Friedel et al., 2001; Korth et al., 1999) within a few hours of HSS arrival at the magnetopause (Denton & Borovsky, 2009). In our study, we will focus on the whole period that is reasonably quiet but perturbed by moderate substorm activity. On July 9 activity picked up with the HSS and the analysis stops on July 10.

2.2 Substorm activity

Figure 1 contains plots of the geomagnetic conditions, including AE (top) and Kp (bottom) geomagnetic indices. The AE index is well-correlated with the occurrence of

157 substorms—events that are known to inject plasma into the inner magnetosphere,
158 either in isolation or during multiple substorm onsets (Mauk and McIlwain 1974;
159 Reeves et al., 1991; Sergeev et al., 1998; Henderson, Reeves, et al., 2006; Henderson,
160 Skoug, et al., 2006; Turner et al., 2015). During this time period, the AE index remains
161 mostly at very low levels, except for two excursions indicative of substorms (June 30
162 and July 3-4). The Kp index (plotted here as a mean value every 8h) and SYM/H index
163 (Figure 1, 4th image) were also at very low levels. The maximum Kp was reached twice
164 on June 30 and July 10 (Kp = 3), and the minimum SYM/H occurred on July 3 (SYM/H=-
165 20 nT). Apart from these excursions, both indices highlight the very low levels of
166 magnetospheric activity (Kp ≤ 2 and SYM/H∼0) during this interval.

167 The substorm activity during this time is more complex than it appears from the
168 AE index and Van Allen Probes. There are a number of substorms (and injections) that
169 can be seen from the electron flux reported from 6 satellites of the LANL GEO
170 constellation in Figure 2. Comparison with Van Allen Probes flux is also provided in the
171 2 bottom panels. Van Allen Probes apogee MLT was ∼9 on July 1. Days of quietness with
172 steady flux are July 1, 5, 6. Small injections occur on July 2 near 12:00 while Probe A was
173 at perigee and Probe B was at very low L and on July 4 while both Probes are in the
174 inner zone. These two injections appear to be single injection followed by drift echoes.
175 July 3 has a longer interval of substorm activity observed both by LANL satellites at GEO
176 and by Van Allen Probes. At the beginning of July 7, we observe another injection that is
177 fairly typical of an isolated substorm, followed by drift echoes. This injection is also
178 visible in the Van Allen Probes data that are located at higher L-shell. Some of these
179 substorms affect the plasmapause location more than others. Substorm injections on
180 July 3 and 7 modify the density and the wave activity as shown in the next subsection.
181 There is also activity on July 8 which perturbation on the density is conversely quite

mild and not well apparent (cf. next section and Figure 3). July 9 has two more isolated substorms when Van Allen Probes were at low L. These substorms did seem to move the plasmapause inward as well. The HSS event starts on July 10 with the beginning of the flux enhancements visible in Figure 2.

2.2 Plasma density

NASA's Van Allen Probes consist of twin spacecraft on near-equatorial elliptic orbits. The orbital period is ~9 hr, the MLAT coverage |MLAT| < 20°, and the orbital apogee is ≈ 6 R_E. Full precession of the apogee through all MLTs occurs approximately every 2 years. In this work, we use the data from two waves instruments, the Electric and Magnetic Field Instrument Suite and Integrated Science (EMFISIS) (Kletzing et al., 2013) and the Electric Fields and Waves (EFW) instrument (Wygant et al., 2013), as well as data from the Magnetic Electron and Ion Spectrometer (MagEIS) particle instrument (Blake et al., 2013), all onboard the Van Allen Probes (Mauk et al., 2013).

The plasma density enters directly in the dispersion relation that controls the strength of wave-particle interactions. An accurate knowledge of its value is therefore important for the computation of the electron diffusion and scattering performed in the next section. For instance, Albert et al. (2020) found that the lifetimes for 1-2 MeV electrons for L=[1.5,2] was a factor of 4-5 times greater using a low-density model than a high-density model. Because plasma density influences so greatly diffusion coefficients, it is a source of a great amount of uncertainty in electron flux prediction (Camporeale et al. 2016). The plasma density for our event period is derived by procedure that combines Van Allen Probes data and models when data are lacking. The density is first either derived directly from the upper hybrid resonance frequency (Kurth et al., 2015) measured by EMFISIS, or when EMFISIS density is unavailable,

derived from spacecraft floating potential data calibrated against plasma densities determined from the upper hybrid resonance frequency (Thaller et al., 2017). Spacecraft floating potential is measured by the EFW instrument. Combining both techniques allows to obtain the density the majority of the time (as shown and discussed below and in Figure 3). Nevertheless, if the density from either technique is unavailable, the procedure automatically replaces the unknown density by the statistical model of Albert (1999) within the plasmasphere and the Sheeley et al. (2001) expression outside. In these cases, the plasmapause location is needed to differentiate between the two models. This is defined from the 100 #/cc level extracted from both EMFISIS and EFW database or, if the 100 #/cc level (+/- 30%) is also undefined, we use the empirical plasmapause model of Carpenter and Anderson (1992) with the knowledge of the Kp* index in order to separate the dense plasma from the low plasma density. When the density is obtained from the measurements, as here in most cases, there is no need for defining a plasmapause in the modeling.

Figure 3(top left) shows the plasma density from 1 to 10 of July 2014. We accumulate all densities which fall into a given time bin i, t in $[t_i, t_i + \Delta t)$, and into a given L bin j, L in $[L_j, L_j + \Delta L]$. This gives a 2-D matrix [t, L], which has a set of values in each cell (i, j). For each cell, we then calculate the mean value of the density (and of all quantity mentioned in the following). We choose a time scale of Δt = 8 h, as a compromise between the time resolution (the lowest minimum time step between perigee and apogee is Δt = 4.5 h.), a day integer fraction, and a not too prohibitive computational time. This discretization gives 30 time samples for 10 days. We also choose to treat 43 points in L shell, from L = 1.3 to L = 5.5 (by steps of ΔL = 0.1), at which values have been averaged over the available latitudes and MLT of the probes, resulting in a fine grid of 43 × 30 = 1290 nodes, within which all models will be evaluated. This

method was first established in Ripoll et al., (2016a, 2017). Figure 3(left) shows that a lack of density measurements occurs below L=1.7, where the density model of Albert et al. (1999) replaces the missing observations, without any impact on this study. We will also show below that the Sheeley et al. (2001) model is never used for this event as the Van Allen Probes density is always defined below L=5.5.

The inner plasmasphere, defined here as a density larger than 100 #/cc, extends up to L~5.5 for the quietest times. Figure 3 (top right) shows the few cells below L=5.5 in which the density level goes below 100 #/cc. During the main substorm activity associated with the AE peaks (Mauk and McIlwain 1974; Reeves et al., 1991; Sergeev et al., 1998; Henderson, Reeves, et al., 2006; Henderson, Skoug, et al., 2006; Turner et al., 2015) occurring during short durations (<8 hours) on July 3, 4, and 5, we observe short local compression or erosion of the plasmasphere down to L~4.5. The incoming HSSs on July 10 is also visible. Comparing Figure 2 and 3 confirms the substorms on July 3 to 4, 7 and 9 affect the density. These perturbations of the plasmasphere by substorm injections have direct consequences on the whistler-mode wave activity and will be discussed further in the next section.

Figure 3 (bottom left) provides an alternative computation of the plasma density based on observations of plasmaspheric hiss (Hartley et al., 2018). This new approach has two direct interests. First, it provides a verification of the density level and a replacement value when direct measurements are unavailable. Though this method does contain some approximations, such as the assumption of parallel propagation, it has been shown to provide results consistent with other methodologies (Hartley et al., 2018). Second, it provides an indicator of the hiss activity; if the density can be inferred from the hiss waves, it follows that hiss must be present at that time and location. We can see that hiss waves were present below L=5 for the whole period, except during the

substorm activity on the July 3 and 4 and before the HSS on July 10. We will confirm these interpretations in the next section from the wave observations. Limitation of the computations to L=5 is not mandatory per se but guarantees greater accuracy of the density values as the plasmasphere erosion and the absence of hiss occurs above L=5, particularly as magnetospheric activity increases.

Figure 3(bottom right) shows the density is always obtained in our study from Van Allen Probes measurements as the last L-shell of the known density largely exceed L=5.5. One can define the plasmapause region as being somewhere between 100 #/cc and 10#/cc. The region of 100 #/cc to 30#/cc highlighted in Figure (bottom right) could be called the denser part of the plasmapause region. This region is often located above L~4.7 for this event, and above L=5 outside of the substorm injection, and is widely spread over L-shell, except at the time of substorm injections. We will show below that this region contains whistler-mode waves, likely whistler-mode hiss waves due to their low mean frequency and to the high density shown in Figure 3(bottom left) (though checking the microscopic structure is beyond the scope of this study), which will contribute to electron scattering in the outer belt.

Malaspina et al. (2018) also found a correlation between whistler-mode hiss wave power and the plasma density (for L>2), independent of geomagnetic activity; hiss power increases with density. For instance, in Ripoll et al., (2019b) this correlation was illustrated for various AE index, i.e. various substorm conditions indicative of the magnetic activity (see also Malaspina et al., 2016). Density and hiss power are thus coupled, with good knowledge of their values at all locations and all times being critical to obtaining the best accuracy.

2.3 Wave properties

We use wave measurements from the EMFISIS instrument, restricting the measurements to right-hand polarized waves with ellipticity (Santolik et al, 2002) above 0.2, and to a frequency range typical for plasmaspheric hiss from 50 Hz to 2 kHz (Santolik et al., 2001; Hartley et al., 2018b). These criteria are still not sufficient to select whistler-mode hiss waves only and can lead to the selection of whistler-mode chorus waves at high L-shell during disturbed time. The knowledge of the density and the plasmapause location can, in turn, help discriminate whether the whistler-mode waves are indeed hiss or chorus. But this task still remains complex when the plasmasphere density is at intermediate levels in the plasmapause region, between ~100 #/cc and ~10#/cc. We overcome that complexity by 1) identifying as best as possible the plasmasphere and, therefore, the hiss location, 2) perform our computation of whistler effects without trying to distinguish whistler-mode hiss waves from whistler-mode chorus waves. The latter task is uncommon and made possible in this work because the knowledge of all wave and plasma properties is locally available such that no statistical model is involved for either statistical hiss or chorus wave properties. It should be noticed that high frequency whistler mode waves occurring in low-density regions (below 30 /cc) are assimilated to chorus waves in this study, although the microscopic structure of these waves has not been checked. The main limitation of our method comes from the upper frequency we impose on the whistler-mode waves (2 kHz), which results in the exclusion of higher frequency waves (e.g. upper band chorus waves) from this analysis. Missing the upper band of the chorus frequency spectrum leads to an underestimation of pitch angle diffusion at low energy (<100 keV) for L>4.5. This is not a concern for this study since we focus on >100 keV electrons.

Figure 4 shows the whistler-mode wave properties for the period of interest, and that enter in the computation of hiss pitch angle diffusion effects (cf. Ripoll et al., 2017

for their definition). Figure 4 (left) shows the mean value of the whistler-mode wave frequency for each node. Figure 4(right) shows mean values of the wave power spectra, accounting for Magnetic Local Time (MLT) dependence of the wave amplitude using the Spasojevic et al. (2015) model. The mean wave vector angle, θ_m, calculated from data obtained by the Singular Value Decomposition method of Santolik et al. (2003), and the mean wave vector width $\Delta\theta_m$ are also plotted in Figure 4. A filamentary temporal structure of both frequency and amplitude hiss wave data is very apparent. The mean frequency shows three populations, two for hiss and one for chorus. The first is between 200–400 Hz and the second is at higher frequencies between 600–800 Hz. Both correspond to whistler-mode hiss waves that occupy most of the domain of the study. Some rare incursions of chorus waves above L=5.2 are visible, with a mean frequency that exceeds ~1000 Hz. These chorus incursions are synchronized with the lowest densities observed in Figure 3. Structures change in time and space in a dynamic and complex way as the satellite orbits around the Earth. Wave amplitudes vary by orders of magnitude. The stronger hiss waves are located in the plasmasphere interior, between L = 2 and L = 4. The mean wave normal angle and mean wave normal width are rather homogeneous, with a moderate global mean value of the wave normal angle close to 40°. In the rare case of large wave normal angles, above ~60°, pitch angle diffusion drastically reduces and electron lifetime increases (Ripoll, Albert, and Cunningham, 2014; Albert, 2017). We find some similarities with the wave observations made in Ripoll et al. (2017) for a quiet event in March 2013.

3. Computation of diffusion coefficients

3.1 Validity of the approximations used in the model

In this study, bounce averaged diffusion coefficients $D_{\alpha 0 \alpha 0}(L, E, \alpha_0, t)$ are computed following the equations of Lyons et al. (1972), which uses both the low frequency ($\omega_m/\omega_{ce0} < 1$) and the dense plasma ($\omega_m\omega_{ce0}/\omega_{pe}^2 \ll 1$) approximations. To demonstrate the validity of these assumptions, these quantities are plotted in Figure 5 (center) and (right). Both of these approximations have been shown to be reliable in the plasmasphere (Albert, 1999; Glauert and Horne, 2005) due to the dense plasma, large magnetic field, and the dominance of low-frequency whistler-mode waves. Furthermore, they have been shown to be more generally applicable to the plasmasphere during quiet times, when the plasmasphere expands out to L~5.5 (Ripoll et al., 2017, 2019a). Figure 5 demonstrates that these approximations still hold during the moderate perturbations brought by substorm activity. Only on July 3rd (date of the largest substorm) and on July 10th (date of the HSS) for L>5.2 (4 cells), are these approximations close to being violated, with $\omega_m\omega_{ce0}/\omega_{pe}^2>0.01$. We note that this may introduce some inaccuracy of our results at these dates and locations. This approximation is applicable primarily due to the low frequency of the whistler-mode waves, which compensate for the low density associated to the erosion of the plasmasphere during the substorm activity. During the various substorms on July 3, 4, and 7, as well as during the HSS on July 10, we note that ω_{pe}/ω_{ce0} (Figure 5, left) drops by a factor ~4, from 20-25 down to ~6, a clear indicator of the plasma density decrease.

3.2 Diffusion coefficients

The computation of the bounce- and drift- averaged equatorial pitch-angle diffusion coefficient is performed for each 8 h interval at each L-shell (0.1 L resolution) based on the observed wave properties described in section 2. Mathematical expressions of the diffusion coefficients can be found in (Lyons et al. 1972; Albert, 1999;

Albert, 2005; Glauert and Horne, 2005) and are not recalled here. Diffusion coefficients are computed for 60 energies (E varying from 0.07 MeV to 6MeV) at every node (t, L), i.e., 75 600 times (43L × 30t × 60E). A grid of 256 pitch angles in [0, 90°] and n cyclotron harmonics is used, with the harmonic number determined by an estimate (Mourenas and Ripoll, 2012). A massively parallel supercomputer is required to generate this database of 19.3M diffusion coefficients, with a total cost of computation of ~12 hours/processor for ~1300 processors, i.e. ~15600 hours for our ~10-day event.

The result is a data-derived, time-varying diffusion coefficient, $D_{\alpha 0 \alpha 0}(t, L, E, \alpha_0)$= $D_{\alpha 0 \alpha 0}(f_m(t,L), \Delta f(t,L), \theta_m(t,L), \Delta\theta(t,L), n_e(t,L), E, \alpha_0)$, which depends on (t, L) through the mean wave frequency, f_m, the wave frequency width, Δf, the mean wave normal angle, θ_m, the wave normal angle width, $\Delta\theta$, and the plasma density, n_e. Dependence on energy, E, and equatorial pitch-angle, α_0, is inherited from the resonance and dispersion relations used for deriving $D_{\alpha 0 \alpha 0}$. Time-varying diffusion coefficients are plotted in Figure 6 at L=3.5 and L=4.5, with each panel showing the first 8h for each day of the event (307 200 values, 1.6% of the database). It is evident that the diffusion coefficients are highly variable from one day to the next. This is due to the variability of the wave properties and the plasma density. Typically, the wave normal angle influences the diffusion profile; a low wave-normal angle produces cyclotron diffusion which increases with pitch angle, whereas an intermediate wave-normal angle produces cyclotron diffusion that is approximately constant with respect to pitch angle. We observe higher diffusion coefficients, for instance on the 07/01 and on 07/05, which coincides with non-perturbed times. It is important to note that wave properties are correlated together as well as correlated with the plasma density as previously discussed (and in Malaspina et al. 2016, 2018; Ripoll et al., 2016a, 2017, 2019a, 2019b). Computing time-varying diffusion coefficients, as done here, allows us to keep all these

correlations. The alternative method (not chosen here) of averaging each wave property and the plasma density separately before plugging them into a single diffusion coefficient, i.e. $D_{\alpha 0 \alpha 0}\left(\widehat{f_m(L)}, \widehat{\Delta f(L)}, \widehat{\theta_m(L)}, \widehat{\Delta\theta(L)}, \widehat{n_e(L)}, E, \alpha_0\right)$ or $D_{\alpha 0 \alpha 0}\left(\widehat{f_m}, \widehat{\Delta f}, \widehat{\theta_m}, \widehat{\Delta\theta}, \widehat{n_e}, E, \alpha_0\right)$ (e.g. Zhu et al., 2019) in which $\widehat{(.)}$ denotes a temporal or both a temporal and a spatial averaging, cannot conserve the various correlations between the various properties and introducing *de facto* an error. Solving for the diffusion coefficients at small time and spatial scales allows us to avoid any artificial numerical smoothing that inevitably occurs if one uses averaged wave and plasma properties.

Figure 7 shows the averaged diffusion coefficients used for the simulation, at 4 selected L-shells. This diffusion coefficient is computed from the temporal average of the 30 time-varying diffusion coefficients at each (L, E, α_0):

$$\widehat{D_{\alpha 0 \alpha 0}}(L, E, \alpha_0) = \left(D_{\alpha 0 \alpha 0}(f_m(t, L), \widehat{\Delta f(t, L)}, \theta_m(t, L), \Delta\theta(t, L), n_e(t, L), E, \alpha_0)\right)$$

Figure 7 shows that pitch angle diffusion occurs at lower energy as L increases. At L=2.5, one can easily distinguish cyclotron diffusion (the upper left green region) from the Landau diffusion above ~75°, both separated by a wide region of extremely weak (Landau) diffusion (in blue). This region of extremely weak diffusion shrinks with increasing L as cyclotron diffusion reaches both higher pitch angles and lower energies.

3.3 Lifetime

Electron lifetimes, i.e. the e-folding time scales, τ, in days, are computed from the averaged diffusion coefficients following the original method of Lyons et al. (1972). That method is discussed and explained in greater detail in Ripoll et al., (2016b) and shall not be recalled here. It has been proven extremely robust when used to generate lifetimes from several millions of diffusion coefficients in Ripoll et al. (2014).

406 The electron lifetime profile is particularly interesting and characteristic when
407 plotted daily in the (L, E) plane (Meredith et al., 2006b; Ripoll et al., 2014a, 2016b;
408 2017). There are two comments of importance that are evident from these lifetimes
409 during our period of interest shown in Figure 7. First, electron lifetimes are similar in
410 both shape and amplitude to those obtained during the quiet period of March 2013. The
411 shape follows a complex and dynamic filamentary structure, directly inherited from the
412 wave properties. Average electron lifetimes are of the order of 1–10 days when waves
413 are active and at the energies where the resonance causes maximal diffusion. The
414 absence of pitch angle diffusion from whistler-mode waves for inner belt electrons
415 below ~800 keV (Fennell et al. 2015) causes lifetimes in excess 100 days (see
416 Claudepierre et al. 2020 for recent apparent lifetimes extracted from Van Allen Probes
417 data). Theoretically, lifetimes can be much larger and the time to reach equilibrium, so
418 that decay is steady enough to be described by lifetimes, can itself be quite large, in
419 particular in the inner belt (Ripoll et al. 2016b). Large lifetimes explain why inner belt
420 electrons below 1 MeV are so stable and can remain trapped for many months. It is
421 worth noting that despite lightning-generated whistlers being commonly observed in
422 the inner belt, with their amplitude recently reported form the Van Allen Probes
423 measurements in (Ripoll et al. 2020b), they are disregarded in this study. This is due to
424 the fact that their amplitudes are typically too weak to contribute significantly to fast
425 losses occurring within 10 days (Meredith et al., 2007, 2009; Ripoll et al., 2019d). For
426 quiet times with a greatly extended plasmasphere, effects on low-energy electrons
427 (<300 keV) extend to the outer belt, to L = 5.5. Such a plasmasphere configuration is
428 essential to understanding the decay of outer belt electrons from whistler-mode waves.
429 Whistler-mode waves predominantly act along a main diagonal line in the (L-shell,
430 Energy) plane, which decreases with increasing L-shell (Lyons and Thorne, 1973).

Electron lifetimes along this diagonal are close to 1 day attesting to strong pitch angle scattering, predominantly due to whistler-mode hiss waves. Electron lifetimes remain low as energy increases from 200 keV up to 2 MeV; at 1 MeV the lifetime is 3.5 days at L=3.0, 9 days at L=4.0, 7 days at L=5.0, and 21 days at L=5.5.

The second comment of importance concerns the two zones that are observable in the lifetime profile, one below L~4.7 and the other above, with low lifetimes seemingly shifted up in energy. In actuality, this is not a shift in energy since the lifetime decreases homogeneously in energy; lifetimes are simply lower. This effect is the net result of various effects acting oppositely. This reduction in electron lifetimes could be directly associated with a decrease in the plasma density. From Figure 3 (top), it is apparent that the lowest density does indeed occur above L~4.7 (cf. the black region). This density decrease is attributed to the increase in the AE index and to the substorm activity, as explained in section 2. Therefore, we may postulate that the moderate substorm activity leads to a lower plasma density in the outer belt, above L~4.7, that in turn lowers the electron lifetime. But evaluating individual diffusion coefficients for L-shell at L=4.8, 4.9, 5., 5.1, by step of 8 hour (Figures not shown), we do not observe a noticeable increase in the diffusion coefficients associated with the substorm injection and attributed to the lowering of the density, though theoretically speaking lowering the density does lower the electron lifetimes (all other parameters unchanged). This scenario is possible, and likely happening to some extent, and could occur for other events. However, we find that pitch angle diffusion is actually lower (higher lifetimes) during the substorm injections, despite the lower plasma density. This is due to the whistler-mode wave amplitude decreases that occur during July 3, 4, 7 and 10, each associated with substorm injections (cf. Figure 2-3). These reductions in wave amplitude contribute to lower pitch angle diffusion, which directly increases electron lifetimes. The

456 decay of the whistler-mode wave amplitude becomes more important on average than
457 the decay of the density. That is, the mean lifetime increases during substorm activity.
458 The decrease in the mean electron lifetime above L~4.7 can be explained by the
459 enhancement of whistler-mode waves during the reasonably quiet times that occur
460 between the substorm injections, such as on July 5 in Figure 6. The substorm activity is
461 weak enough that the moderate compression (or moderate erosion) of the
462 plasmasphere does not cause the whistler-mode hiss waves to vanish with it. We can
463 conclude that pitch angle diffusion by whistler-mode waves has various characteristic
464 features of opposite effect; first, during the injection, there is a lowering of the whistler-
465 mode wave amplitude which increases lifetimes and also a decay of the density which
466 lowers lifetimes, and, second, in between the substorm perturbations, there is a
467 strengthening of the whistler-mode waves which lowers the mean lifetime. When
468 combined, all three effects lead to a mean enhancement of loss above L~4.7 in our event.
469 Finally, the density drop associated with the substorm injections is also likely to cause
470 changes in the wave properties such as the mean frequency, at least when the chorus
471 incursion occurs leading to a higher mean frequency. Would these features still be
472 apparent if we had used statistical diffusion coefficients (or lifetimes) that cannot keep
473 all plasma and wave properties correlated?
474
475 **4. Observations and Fokker-Planck simulations**
476 3.1 Van Allen Probes flux observations
477 Figure 8 shows 27 electron flux snapshots observed by the Van Allen Probes in
478 the (L, E) plane, taken each outbound pass (every ~9h) where data are available from 30
479 June 2013 to 9 July 2013. These snapshots are constructed from MagEIS observations
480 (Blake et al., 2013) with the Level 2 spin-averaged flux interpolated onto a regular fixed

grid in L. Spin-averaged fluxes have been shown to accurately represent the omnidirectional flux that can be generated using Level 3 MagEIS measurements (Ripoll et al., 2019a). Note that the background correction algorithm of Claudepierre et al. (2015) has been applied to the MagEIS electron flux measurements shown here.

The snapshots of Figure 8 are similar to the original format presented in Reeves et al. (2016), and also those used in Ripoll et al. (2016a, 2016b, 2017, 2019a, 2019b). The main substorm injection of electrons is apparent on July 3, with higher flux in the outer belt observed below 200 keV (e.g. Turner et al., 2015). The substorm of July 4 is too weak to be visible; the flux of new incoming electrons at L~5 is likely balanced by the strong loss of the older outer belt electrons below 200 keV. The substorm on July 7 leads to a slight increase of the flux at the lowest energies. The high-speed stream injection at the end of the event, on July 10, is also visible. There is a good concordance between the observed flux decay and the low electron lifetimes in the (L, E) plane. The slot region progressively enlarges, and the outer belt flux drastically decays during this 10-day period as substorm injections modify only the low energy structure. Since the beginning of the event, there is a characteristic quiet time S-shape to the inner boundary of the outer belt when drawn in the (L, E) plane reported by Reeves et al. (2016) and computed in Ripoll et al. (2016a, 2016b, 2017, 2019a, 2019b). When most of the high energy part of the outer belt has decayed after 10 days, with little flux left (omitting low energy injections below 200 keV), there exists a remnant pocket of trapped electrons, for L in [4.7, 5.2] and E in [1, 2] MeV, that constitutes the remains of the upper loop of the 'S', first discussed in Ripoll et al. (2019a).

3.2 Simulations

505 The temporal evolution of the gyro, bounce, and drift phase-averaged phase
506 space density, $f(t, L, E, \alpha_0)$, in the presence of pitch-angle diffusion can be described by
507 (*Schulz and Lanzerotti*, 1974; *Shprits et al.*, 2008):

508 $$\frac{\partial f}{\partial t} = \frac{1}{G}\frac{\partial}{\partial \alpha_0}\Big|_{L,E}\left(G\widehat{D_{\alpha_0\alpha_0}}\frac{\partial f}{\partial \alpha_0}\Big|_{L,E}\right) \quad (1)$$

509 with $\widehat{D_{\alpha_0\alpha_0}}$ computed in section 3 (cf. Figure 7) and $G = T(\alpha_0)\sin(2\alpha_0)$. T($\alpha_0$) is
510 proportional to the bounce period evaluated at the equatorial pitch-angle, α_0. We use
511 $f(\alpha_{0,lc}) = 0$ at the loss cone, which itself is computed from a dipolar magnetic field. A
512 Newman boundary condition is used at 90°, $\frac{\partial f(t,\alpha_0)}{\partial \alpha_0} = 0$. Equation (1) neglects radial
513 diffusion and off-diagonal terms in the diffusion tensor. The numerical method and code
514 are described in Réveillé et al. (2001). The absence of radial diffusion makes it
515 impossible to solve for any injections associated with the substorm activity. In addition,
516 energy diffusion is neglected in this study since energy diffusion coefficients are
517 negligible for whistler mode hiss waves (e.g. Albert, 2008) on which that study focuses.
518 Only scattering from pitch angle diffusion, and how the effects of whistler-mode waves
519 are affected by the substorm activity, are investigated in this section.

520 Figure 9 shows the omnidirectional flux, i.e. the phase space density integrated
521 with respect of pitch angle, solution of Equation 1 at each L-shell and energy. In this first
522 numerical experiment, we choose the initial condition as $f(t = 0, L, E) = cos^2(\alpha_{0,lc}) -$
523 $cos^2(\alpha_0)$. This function guarantees a smooth transition at the loss cone where f=0 and is
524 homogeneous with respect to energy. This allows all particles to decay from their initial
525 state and for us to better understand and quantify their loss. Results immediately show
526 the two distinct regions, below and above L~4.7, with the region above L~4.7 showing
527 more important scattering, as discussed in section 3.3. Interactions with whistler-mode
528 waves are particularly strong below 150 keV for L>3.5, with the omnidirectional flux

529 decaying by more than 5 orders of magnitude in 10 days (Figure 9 is saturated at level -5
530 in order to see details at higher energies). This low energy region (<150 keV) is highly
531 dynamic; with injections required to be both numerous and fast in order to bring new
532 electrons to lower L-shells and overcome the losses due to whistler-mode waves, as
533 seen in the observations in Figure 8. More generally, Figure 9 describes the decay
534 associated with the formation of a wide slot region. Above L~4.7, we see a significant
535 decay of the omnidirectional flux in the outer belt up to ~1 MeV, similar to observations.
536 Whistler-mode waves have little effect on the remnant pocket of electrons observed in
537 Figure 8 at L in [4.7, 5.2] for E in [1, 2] MeV, with the omnidirectional flux decaying by
538 barely half an order of magnitude in the simulations.

539 The second numerical experiment uses the same pitch angle profile, this time
540 combined with the energy spectrum from the MagEIS spin-averaged L2 flux on the
541 06/30/2014 (6.54am-11.31am) (cf. first panel of Figure 8). The results of this
542 simulation are plotted in Figure 10, and are the best representation of the losses that we
543 believe are occurring in the slot region and in the outer belt during this event. Various
544 important features are apparent: i) the inner belt, defined as ~1 MeV electrons below
545 L=2 (at the edge of the simulation domain) or ~100 keV electrons below L=3.5, is
546 unaffected by whistler-mode waves; ii) the slot region is formed in ~10 days along the
547 diagonal and is primarily driven by pitch angle diffusion caused by whistler-mode waves
548 (cf. early observations of 35-560 keV electrons from Lyons and Williams (1975)); iii) the
549 outer belt flux decays strongly below ~1 MeV; iv) three complex substorm conditions
550 (cf. section 3) explain why the significant loss reaches up to 1 MeV electrons in the outer
551 belt; v) the remnant pocket of trapped electrons (L in [4.7, 5.2] for E in [1, 2] MeV)
552 decays very slowly, extending to L=5.5 in the simulation due to lack of outward radial
553 diffusion, and becomes increasingly apparent as the outer belt decays; and vi) the

injections of low energy electrons (below ~150 keV and absent of the simulations) associated with substorm activity (up to 300 keV for the strongest substorm) are required to be numerous and fast (e.g. Friedel et al., 1996; Turner et al., 2015) to compensate the intense loss. Finally, comparing the results of Figure 10 with the observations of Figure 8, we see qualitative agreement for both the daily enlargement of the slot and for the significant reduction of the outer belt. Reproduction of these key features is highly encouraging, and demonstrates that this method has the ability to model reasonably electron scattering during quiet time dynamics, perturbed (or not) by moderate substorm activity.

The main limitations of this study relate to; i) the lack of inward transport (usually modeled by radial diffusion) that does not allow reproduction of the substorm injections, ii) the approximations used in the diffusion coefficients (cf. section 3.1), and iii) the magnetic local time (MLT) description that is subsequently discussed. The measurements of frequencies and wave normal angles used here are made locally in MLT, though they are applied to all MLTs. Only the wave amplitude is rescaled by the MLT dependence given by Spasojevic et al. (2015). We believe variation of the wave properties (frequency and mean wave normal angle) to have only minor effects (unless changes are drastic, which is possible [Hartley et al., 2018b]). However, variations in the plasma density with MLT, and the possible development of higher frequency whistler-mode waves, i.e. chorus, in regions of lower density (cf. Figure 3), could affect the accuracy of these simulations since decaying plasma density, caused by substorm activity, is found to have important repercussions. Another caveat of the method is that if the inward motion of the plasmapause is localized where we observe it (or if it is only an apparent motion because of field line stretching) then most of the electron drift orbit is still in the plasmasphere and experiences whistler-mode hiss in a way it may not have

579 a significant effect on the drift-averaged pitch angle diffusion. Both of these problems
580 have no current solution since they are related to the uniqueness of the observation at a
581 given MLT and the absence of availability of any other, leading to speculations about
582 possible situation scenarios along the drift. Finally, there could be acceleration occurring
583 in the rare regions of wave intensification identified in Figure 4 and in the low-density
584 regions highlighted in Figure 3, but the phenomena are too limited in space or/and in
585 time to believe they would significantly matter for this event.

586 The alternative of using statistical models sorted in MLT has little chance of
587 increasing accuracy. Validation would also be an issue as the observed fluxes would be
588 measured at the same MLT. What is encouraging is the synchronization of global indices
589 (like AE here) with local observations, which goes in favor of the generalization of the
590 observations. On the other hand, the location of the whistler-mode waves, which are not
591 uniformly distributed over MLT, is an issue that unavoidably requires the introduction
592 of an MLT-dependence. The only viable alternative, which does not yet exist, is multiple
593 synchronized measurements at various MLT and at fixed L-shell. It is hoped that new
594 radiation belt missions could aim to resolve this issue (e.g. Millan et al., 2019; Ripoll et
595 al., 2020). For now, the only viable approach is to include these necessary
596 approximations in our models and to quantify the accuracy of the results against
597 observations of the decaying radiation belt flux, as it has been done in this study.

598

599 **5. Conclusions**

600 In this work we study the dynamics of radiation belt electrons during a
601 geomagnetically reasonably quiet period perturbed by moderate substorm activity and
602 preceding a high-speed stream (HSS), with the aim of obtaining a global description of
603 the pitch angle scattering occurring in the radiation belts in L-shell [2, 6], and energy

[0.1, 10] MeV. The goal is to assess whether the event-driven methodology, which has been successfully applied for quiet conditions (Ripoll et al., 2016a, 2017, 2019a, 2019b), can also obtain a high degree of accuracy when the radiation belts are perturbed by moderate substorm activity.

For the event studied we show that the plasmasphere extends up to and beyond L = 5, which provides favorable conditions for whistler-mode waves reaching out, and scattering, outer belt electrons. Substorm injections result in low density plasma extending down to L~4.5, although these periods last less than 8h. Whistler-mode waves, mostly plasmaspheric hiss, predominantly act along a main diagonal line in the (L, E) plane, decreasing in energy with increasing L-shell. This diagonal is well marked for quiet events, but shifts up in energy at L~4.7 in this case due to the substorm activity, thus allowing the scattering of up to 1 MeV electrons in the outer belt. Whistler-mode waves drive major loss phenomena which contributes to both the creation of a wide slot region and significant decay of the outer radiation belts below 1 MeV. A good qualitative agreement is found between the observed daily flux from the Van Allen Probes and the computed flux from quasi-linear resonant interactions between electrons and whistler-mode waves.

A main result of this study, brought thanks to the high temporal and spatial resolution of the event-specific pitch angle scattering model in use, is the mean enhancement of the electron pitch angle scattering above L~4.7, which we attribute to substorm activity. We have demonstrated that the observed substorm activity coincides with a short diminution of the plasmaspheric density, in a way that is moderate enough to conserve a plasmaspheric density of ~100 #/cc, or higher, at L=5.5 at times different than the injection time (+/-4h). This has two direct consequences. First, the conservation of the plasmasphere at high L-shell (above 5) allows whistler-mode hiss

waves to remain, exist, and continue contributing to the lowering of the flux level in the outer belt. Second, while the lowering of the density associated with the substorm could increase pitch angle diffusion via wave-particle interactions, we find that this effect does not compensate the whistler-mode wave amplitude decay, which occurs simultaneously during the substorm injections. That is, pitch angle diffusion actually becomes weaker during the substorm injections (+/-4h). However, whistler-mode waves are enhanced in the periods between the substorm injections, due to the widely extended plasmasphere out to, and above, L=5.5. The combination of these opposing effects leads to pitch angle scattering by whistler-mode waves that is, on average over the 10-day period, enhanced above L ~4.7. This allows the scattering of up to 1 MeV electrons in the outer belt but is not sufficient to significantly decay the remnant pocket of relativistic electrons between 1 and 2 MeV located at L in [4.7, 5.2], for which both observations and simulations show an omnidirectional flux that decays only slightly in 10 days.

Acknowledgments.

This work was performed under the auspices of an agreement between CEA/DAM and NNSA/DP on cooperation on fundamental science. The authors acknowledge the International Space Sciences Institute (ISSI) and the participants in a 2020 ISSI workshop. Part of the research presented in this article was supported by the Laboratory Directed Research and Development program of Los Alamos National Laboratory under project number 20180731ER. Work at Iowa is performed under the support of JHU/APL contract 921647 under NASA Prime contract NAS5-01072. Work at CU/LASP is supported by NASA grant 80NSSC18K1034. O.S. acknowledges support from the Czech Academy of Sciences Praemium Academiae award and from the MEYS grant LTAUSA17070. Processing and analysis of the [HOPE, MagEIS, REPT, or ECT] data was

supported by Energetic Particle, Composition, and Thermal Plasma (RBSP-ECT) investigation funded under NASA's Prime contract no. NAS5-01072. All RBSP-ECT data are publicly available at the Web site http://www.RBSP-ect.lanl.gov/

References

Albert, J.M. (1999), Analysis of quasi-linear diffusion coefficients, J. Geophys. Res. 104, 2419.

Albert, J. M. (2008), Efficient approximations of quasi-linear diffusion coefficients in the radiation belts, J. Geophys. Res., 113, A06208, doi:10.1029/2007JA012936.Albert, J. M. (2017), Quasi-linear diffusion coefficients for highly oblique whistler mode waves, J. Geophys. Res. Space Physics, 122, 5339–5354, doi:10.1002/2017JA024124.

Albert, J. M., Starks, M. J., Selesnick, R. S., Ling, A. G., O'Malley, S., & Quinn, R. A. (2020). VLF transmitters and lightning-generated whistlers: 2. Diffusion of radiation belt electrons. Journal of Geophysical Research: Space Physics, 125, e2019JA027030. https:// doi.org/10.1029/2019JA027030

Baker, D. N., S. G. Kanekal, V. C. Hoxie, M. G. Henderson, X. Li, H. E. Spence, S. R. Elkington, R. H. W. Friedel, J. Goldstein, M. K. Hudson, G. D. Reeves, R. M. Thorne, C. A. Kletzing, S. G. Claudepierre, A Long-Lived Relativistic Electron Storage Ring Embedded in Earth's Outer Van Allen Belt, Science 12 Apr 2013, Vol. 340, Issue 6129, pp. 186-190, DOI: 10.1126/science.1233518

Blake, J. B., Carranza, P. A., Claudepierre, S. G., Clemmons, J. H., Crain, W. R., Dotan, Y., et al. (2013). The Magnetic Electron Ion Spectrometer (MagEIS) instruments aboard the Radiation Belt Storm Probes (RBSP) spacecraft. Space Science Reviews, 179(1-4), 383–421. https://doi.org/10.1007/s11214-013-9991-8

678 Borovsky, J. E., & Denton, M. H. (2009). Relativistic electron dropouts and recovery: A
679 superposed-epoch study of the magnetosphere and the solar wind. Journal of
680 Geophysical Research, 114, A02201. https://doi.org/10.1029/2008JA013128

681 Borovsky, J. E., & Denton, M. H. (2010). On the heating of the outer radiation belt to
682 produce high fluxes of relativistic electrons: Measured heating rates at geosynchronous
683 orbit for high-speed stream-driven storms. Journal of Geophysical Research, 115,
684 A12206. https://doi.org/ 10.1029/2010JA015342

685 Borovsky, J. E., & Denton, M. H. (2016). Compressional perturbations of the dayside
686 magnetosphere during high-speed-stream-driven geomagnetic storms. Journal of
687 Geophysical Research: Space Physics, 121, 4569–4589.
688 https://doi.org/10.1002/2015JA022136

689 Camporeale, E., Y. Shprits, M. Chandorkar, A. Drozdov, and S. Wing (2016), On the
690 propagation of uncertainties in radiation belt sim- ulations, Space Weather, 14, 982–992,
691 doi:10.1002/2016SW001494.

692 Carpenter, D. L., and R. R. Anderson (1992), An ISEE/whistler model of equatorial
693 electron density in the magnetosphere, J. Geophys. Res., 97, 1097–1108,
694 doi:10.1029/91JA01548.

695 Claudepierre, S. G., et al. (2015), A background correction algorithm for Van Allen Probes
696 MagEIS electron flux measurements, J. Geophys. Res., in press,
697 doi:10.1002/2014JA020876

698 Denton, M. H., & Borovsky, J. E. (2009). The superdense plasma sheet in the
699 magnetosphere during high-speed-stream-driven storms: Plasma transport timescales.
700 Journal of Atmospheric and Solar - Terrestrial Physics, 71, 1045–1058.
701 https://doi.org/10.1016/j.jastp.2008.04.023

Denton, M. H., & Borovsky, J. E. (2012). Magnetosphere response to high-speed solar-wind streams: A comparison of weak and strong driving and the importance of extended periods of fast solar wind. Journal of Geophysical Research, 117, A00L05. https://doi.org/10.1029/2011JA017124

Denton, M. H., & Borovsky, J. E. (2017). The response of the inner magnetosphere to the trailing edges of high-speed solar-wind streams. Journal of Geophysical Research, 122, 501–516. https://doi.org/10.1002/2016JA023592

Denton, M. H., Henderson, M. G., Jordanova, V. K., Thomsen, M. F., Borovsky, J. E., Hartley, D. P., & Pitchford, D. (2016). An improved empirical model of electron and ion fluxes at geosynchronous orbit based on upstream solar wind conditions. Space Weather, 14, 511–523. https://doi.org/10.1002/2016SW001409

Denton, M. H., Thomsen, M. F., Reeves, G. D., Larsen, B. A., Henderson, M. G., Jordanova, V. K., ... Spence, H. A. (2017). The evolution of the plasma sheet ion composition: Storms and recoveries. Journal of Geophysical Research: Space Physics, 122. https://doi.org/10.1002/2017JA024475

Fennell, J. F., Claudepierre, S. G., Blake, J. B., O'Brien, T. P., Clemmons, J. H., Baker, D. N., et al. (2015). Van Allen Probes show that the inner radiation zone contains no MeV electrons: ECT/MagEIS data. Geophysical Research Letters, 42, 1283–1289. https://doi.org/10.1002/2014GL062874

Friedel, R. H. W., A. Korth, and G. Kremser (1996), Substorm onsets observed by CRRES: Determination of energetic particle source regions, J. Geophys. Res., 101(A6), 13,137–13,154, doi:10.1029/96JA00399.

724 Friedel, R. H. W., Korth, H., Henderson, M. G., Thomsen, M. F., & Scudder, J. D. (2001).
725 Plasma sheet access to the inner magnetosphere. Journal of Geophysical Research, 106,
726 5845–5858.

727 Glauert, S. A., and R. B. Horne (2005), Calculation of pitch angle and energy diffusion
728 coefficients with the PADIE code, J. Geophys. Res., 110, A04206,
729 doi:10.1029/2004JA010851.

730 Hartley, D. P., Denton, M. H., Green, J. C., Onsager, T. G., Rodriguez, J. V., and Singer, H.
731 J. (2013), Case studies of the impact of high-speed solar wind streams on the electron
732 radiation belt at geosynchronous orbit: Flux, magnetic field, and phase space density, *J.*
733 *Geophys. Res. Space Physics*, 118, 6964– 6979, doi:10.1002/2013JA018923.

734 Hartley, D. P., Kletzing, C. A., De Pascuale, S., Kurth, W. S., & Santolík, O. (2018a),
735 Determining plasmaspheric densities from observations of plasmaspheric hiss. Journal
736 of Geophysical Research: Space Physics, 123, 6679–6691.
737 https://doi.org/10.1029/2018JA025658

738 Hartley, D. P., Kletzing, C. A., Santolík, O., Chen, L., & Horne, R. B. (2018b). Statistical
739 properties of plasmaspheric hiss from Van Allen Probes observations. Journal of
740 Geophysical Research: Space Physics, 123, 2605–2619.
741 https://doi.org/10.1002/2017JA024593

742 Henderson, M. G., Reeves, G. D., Skoug, R., Thomsen, M. F., Denton, M. H., Mende, S. B., ...
743 Singer, H. (2006). Magnetospheric and auroral activity during the April 18, 2002
744 sawtooth event. Journal of Geophysical Research, 111, A01S90.
745 https://doi.org/10.1029/2005JA011111

746 Henderson, M. G., Skoug, R., Donovan, E., Thomsen, M. F., Reeves, G. D., Denton, M. H., ...
747 Frank, L. A. (2006). Substorms during the August 10–11 sawtooth event. Journal of
748 Geophysical Research, 111, A06206. https://doi.org/10.1029/2005JA011366

749 Kletzing, C. A., Kurth, W. S., Acuna, M., MacDowall, R. J., Torbert, R. B., Averkamp, T., et al.
750 (2013). The electric and magnetic field instrument suite and integrated science
751 (EMFISIS) on RBSP. Space Science Reviews, 179(1-4), 127–181.
752 https://doi.org/10.1007/s11214-013-9993-6

753 Korth, H., Thomsen, M. F., Borovsky, J. E., & McComas, D. J. (1999). Plasma sheet access to
754 geosynchronous orbit. Journal of Geophysical Research, 104, 25,047–25,061.

755 Kurth, W. S., De Pascuale, S., Faden, J. B., Kletzing, C. A., Hospodarsky, G. B., Thaller, S., &
756 Wygant, J. R. (2015). Electron densities inferred from plasma wave spectra obtained by
757 the waves instrument on Van Allen Probes. Journal of Geophysical Research: Space
758 Physics, 120, 904–914. https://doi.org/10.1002/2014JA020857

759 Lyons, L. R., and R. M. Thorne (1973), Equilibrium structure of radiation belt electrons, J.
760 Geophys. Res., 78(13), 2142–2149, doi:10.1029/ JA078i013p02142.

761 Lyons, L. R., and D. J. Williams, The storm and post-storm evolution of energetic (35-560
762 keV) radiation belt electrons, J. Geophys. Res., 80, 3985, 1975.

763 Ma, Q., et al. (2016), Characteristic energy range of electron scattering due to
764 plasmaspheric hiss, J. Geophys. Res. Space Physics, 121, 11,737–11,749,
765 doi:10.1002/2016JA023311.

766 Malaspina, D. M., Jaynes, A. N., Boulé, C., Bortnik, J., Thaller, S. A., Ergun, R. E., et al.
767 (2016). The distribution of plasmaspheric hiss wave power with respect to plasmapause

location. Geophysical Review Letters, 43, 7878–7886. https://doi.org/10.1002/2016GL069982

Malaspina, D. M., Ripoll, J.-F., Chu, X., Hospodarsky, G., & Wygant, J. (2018). Variation in plasmaspheric hiss wave power with plasma density. Geophysical Research Letters, 45(18), 9417–9426. https://doi.org/10.1029/2018GL078564

Mauk, B. H., and C. E. McIlwain (1974) Correlationof Kp With the Substorm-Injected Plasma Boundary, Journal of Geophysical Research, Vol. 79, N 22, p 3193-3196.

Mauk, B. H., N. J. Fox, S. G. Kanekal, R. L. Kessel, D. G. Sibeck, and A. Ukhorskiy (2013), Science objectives and rationale for the Radiation Belt Storm Probes mission, Space Sci. Rev., 179(1–4), 3–27, doi:10.1007/s11214-012-9908-y.

Meredith, N. P., Horne, R. B., Glauert, S. A., & Anderson, R. R. (2007). Slot region electron loss timescales due to plasmaspheric hiss and lightning‐generated whistlers. Journal of Geophysical Research, 112, A08214. https://doi.org/10.1029/2007JA012413

Meredith, N. P., Horne, R. B., Glauert, S. A., Baker, D. N., Kanekal, S. G., & Albert, J. M. (2009). Relativistic electron loss timescales in the slot region. Journal of Geophysical Research, 114, A03222. https://doi.org/10.1029/2008JA013889

Millan, R. M., R. von Steiger, M. Ariel, S. Bartalev, M. Borgeaud, S. Campagnola, J. C. Castillo-Rogez, R. Fléron, V. Gass et al. (2019), Small satellites for space science A COSPAR scientific roadmap, Advances in Space Research 64, 1466–1517, https://doi.org/10.1016/j.asr.2019.07.035

Reeves, G. D. , R. D. Belian, AND T. A. Fritz (1991), Numerical Tracing of Energetic Particle Drifts in a Model Magnetosphere, Vol. 96, No. A8, Pages 13,997-14,008.

Reeves, G. D., Spence, H. E., Henderson, M. G., Morley, S. K., Friedel, R. H. W., Funsten, H. O., et al. (2013). Electron acceleration in the heart of the Van Allen radiation belts. Science, 341(6149), 991–994. https://doi.org/10.1126/science.1237743

Reeves, G. D., Friedel, R. H. W., Larsen, B. A., Skoug, R. M., Funsten, H. O., Claudepierre, S. G., et al. (2016). Energy‐dependent dynamics of keV to MeV electrons in the inner zone, outer zone, and slot regions. Journal of Geophysical Research: Space Physics, 121, 397–412. https://doi.org/10.1002/2015JA021569

Réveillé, T., Bertrand, P., Ghizzo, A., Simonet, F., & Baussart, N. (2001). Dynamic evolution of relativistic electrons in the radiation belts. Journal of Geophysical Research, 106(A9), 18,883–18,894. https://doi.org/10.1029/2000JA900177

Ripoll, J.-F., J. M. Albert, and G. S. Cunningham (2014), Electron lifetimes fromnarrowband wave-particle interactions within the plasmasphere, J. Geophys. Res. Space Physics, 119, doi:10.1002/2014JA020217.

Ripoll, J.-F., et al. (2016), Reproducing the observed energy-dependent structure of Earth's electron radiation belts during storm recovery with an event-specific diffusion model, Geophys. Res. Lett., 43, 5616–5625, doi:10.1002/2016GL068869.

Ripoll, J.-F., V. Loridan, G. S. Cunningham, G. D. Reeves, and Y. Y. Shprits (2016b), On the time needed to reach an equilibrium structure of the radiation belts, J. Geophys. Res. Space Physics, 121, 7684–7698, doi:10.1002/2015JA022207.

Ripoll, J.-F., O. Santolík, G. D. Reeves, W. S. Kurth, M. H. Denton, V. Loridan, S. A. Thaller, C. A. Kletzing, and D. L. Turner (2017), Effects of whistler mode hiss waves in March 2013, J. Geophys. Res. Space Physics, 122, doi:10.1002/2017JA024139.

812 Ripoll, J. ‐ F., Claudepierre, S., Ukhorskiy, S., Colpitts, C., Li, X., Fennell, J., & Crabtree, C.
813 (2020). Particle Dynamics in the Earth's Radiation Belts: Review of Current Research
814 and Open Questions. Journal of Geophysical Research: Space Physics, 125,
815 e2019JA026735. https://doi.org/ 10.1029/2019JA026735

816 Ripoll, J.-F., Loridan, V., Denton, M. H., Cunningham, G., Reeves, G., Santolík, O., et al.
817 (2019a). Observations and Fokker-Planck simulations of the L-shell, energy, and pitch
818 angle structure of Earth’s electron radiation belts during quiet times. Journal of
819 Geophysical Research: Space Physics, 124. https://doi. org/10.1029/2018JA026111

820 Ripoll, J.-F., M Denton, V Loridan, O Santolík, D Malaspina, D P Hartley, G S Cunningham,
821 G Reeves, S Thaller, D L Turner, J F Fennell, A Y Drozdov, J S Cervantes Villa, Y Y Shprits,
822 X Chu, G Hospodarsky, W S Kurth, C A Kletzing, J Wygant, M G Henderson and A Y
823 Ukhorskiy (2019b), How whistler mode hiss waves and the plasmasphere drive the
824 quiet decay of radiation belts electrons following a geomagnetic storm, Journal of
825 Physics, Proceeding Series, accepted.

826 Ripoll, J. ‐ F., Farges, T., Lay, E. H., & Cunningham, G. S. (2019d). Local and statistical
827 maps of lightning ‐ generated wave power density estimated at the Van Allen Probes
828 footprints from the World ‐ Wide Lightning Location Network database. Geophysical
829 Research Letters, 46. https://doi.org/ 10.1029/2018GL081146

830 Ripoll, J. ‐ F., Farges, T., Malaspina, D. M., Lay, E. H., Cunningham, G. S., Hospodarsky, G.
831 B., et al. (2020). Analysis of electric and magnetic lightning-generated wave amplitudes
832 measured by the Van Allen Probes. Geophysical Research Letters, 47, e2020GL087503.
833 https://doi.org/ 10.1029/2020GL087503

834 Santolik, O., M. Parrot, L.R.O. Storey, J. Pickett, and D. A. Gurnett (2001), Propagation
835 analysis of plasmaspheric hiss using Polar PWI measurements, Geophys. Res. Lett., 28,
836 1127-1130.

837 Santolik, O., J. S. Pickett, D. A. Gurnett, and L. R. O. Storey (2002), Magnetic component of
838 narrow-band ion cyclotron waves in the auroral zone, J. Geophys. Res., 107(A12),
839 1444,doi:10.1029/2001JA000146.

840 Santolik, O., M. Parrot, and F. Lefeuvre, Singular value decomposition methods for wave
841 propagation analysis, Radio Sci., 38(1), 1010, doi:10.1029/2000RS002523, 2003.

842 Schulz, M., and L. Lanzerotti (1974), Particle Diffusion in the Radiation Belts, Springer,
843 New York.

844 Sergeev, V.A., M. A. Shukhtina R., Rasinkangas., A. Korth, G.D. Reeves, H. J. Singer, M. F.
845 Thomsen and L. I. Vagin (1998), Event study of deep energetic particle injections during
846 substorm, J. Geophys. Res., Vol. 103,No. A5, Pages 9217-9234.

847 Spasojevic, M., Y. Y. Shprits, and K. Orlova (2015), Global empirical models of
848 plasmaspheric hiss using Van Allen Probes, J. Geophys. Res. Space Physics, 120, 10,370–
849 10,383, doi:10.1002/2015JA021803.

850 Sheeley, B. W. M., B. Moldwin, H. K. Rassoul, and R. R. Anderson (2001), An empirical
851 plasmasphere and trough densitymodel: CRRES observations, J. Geophys. Res., 106,
852 25,631–25,641, doi:10.1029/2000JA000286.

853 Shprits, Y. Y., S. R. Elkington, N. P. Meredith, and D. A. Subbotin (2008a), Review of
854 modeling of losses and sources of relativistic electrons in the outer radiation belt I:
855 Radial transport, J. Atmos. Solar-Terr. Phys., 70, 1679, doi:10.1016/j.jastp.2008.06.008.

856 Thaller, S. A., et al. (2015), Van Allen probes investigation of the large-scale duskward
857 electric field and its role in ring current formation and plasmasphere erosion in the 1
858 June 2013 storm, J. Geophys. Res. Space Physics, 120, 4531–4543,
859 doi:10.1002/2014JA020875.

860 Turner, D. L., et al. (2015), Energetic electron injections deep into the inner
861 magnetosphere associated with substorm activity, Geophys. Res. Lett., 42, 2079–2087,
862 doi:10.1002/2015GL063225.

863 Wygant, J. R., et al. (2013), The electric field and waves instruments on the radiation belt
864 storm probes mission, Space Sci. Rev., 179(1–4), 183–220, doi:10.1007/s11214-013-
865 0013-7.

866 Zhu H., Y. Y. Shprits, M. Spasojevic, A. Y. Drozdov (2019), New hiss and chorus waves
867 diffusion coefficient parameterizations from the Van Allen Probes and their effect on
868 long-term relativistic electron radiation-belt VERB simulations, Journal of Atmospheric
869 and Solar–Terrestrial Physics 193, 105090,
870 https://doi.org/10.1016/j.jastp.2019.105090.

871

872

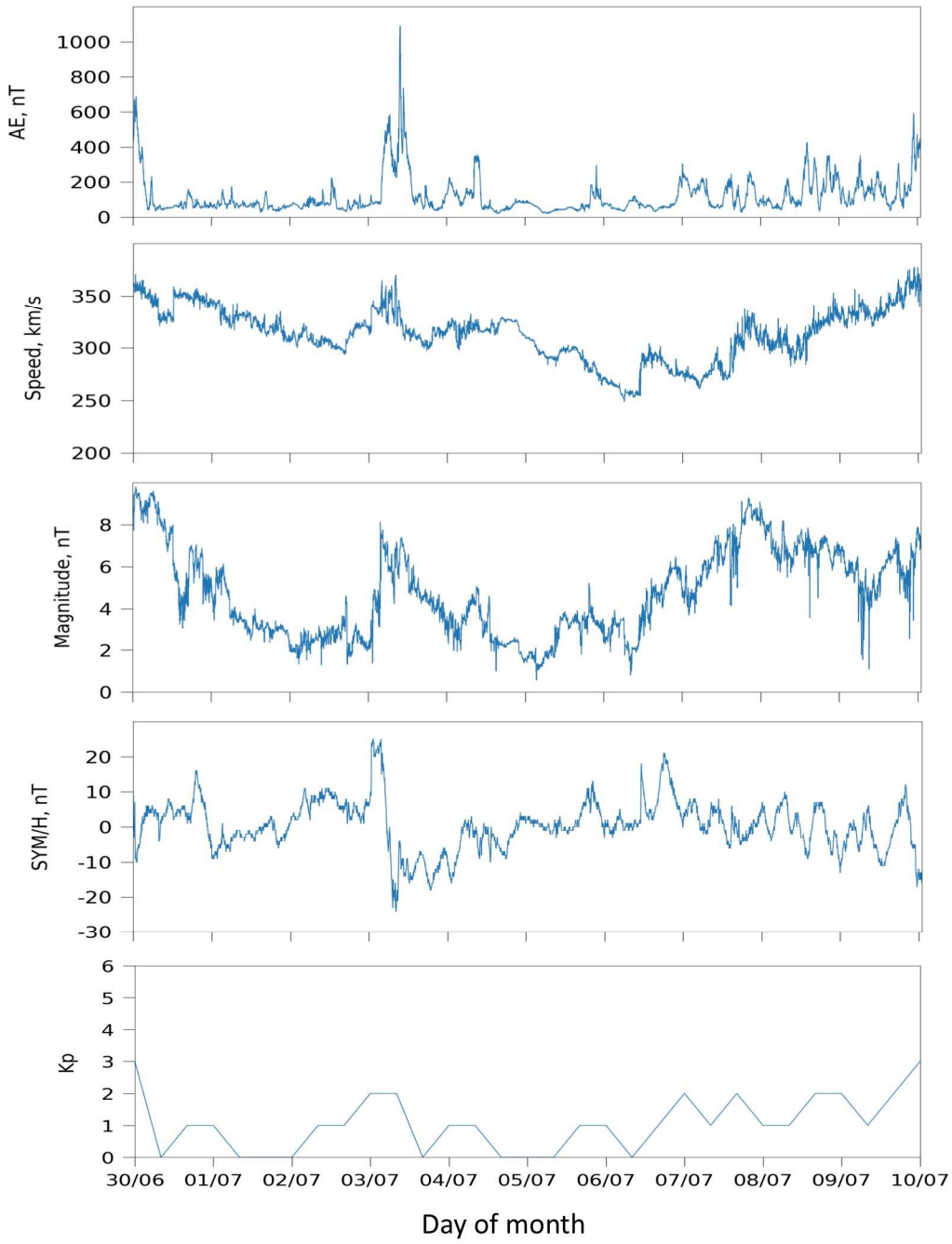

Figure 1: From top to bottom: AE index, solar wind flow speed, interplanetary magnetic field magnitude average, SYM/H index (source https://omniweb.gsfc.nasa.gov/). Averaged Kp index taken per period of 8 hours between June 30 and July 10 2014.

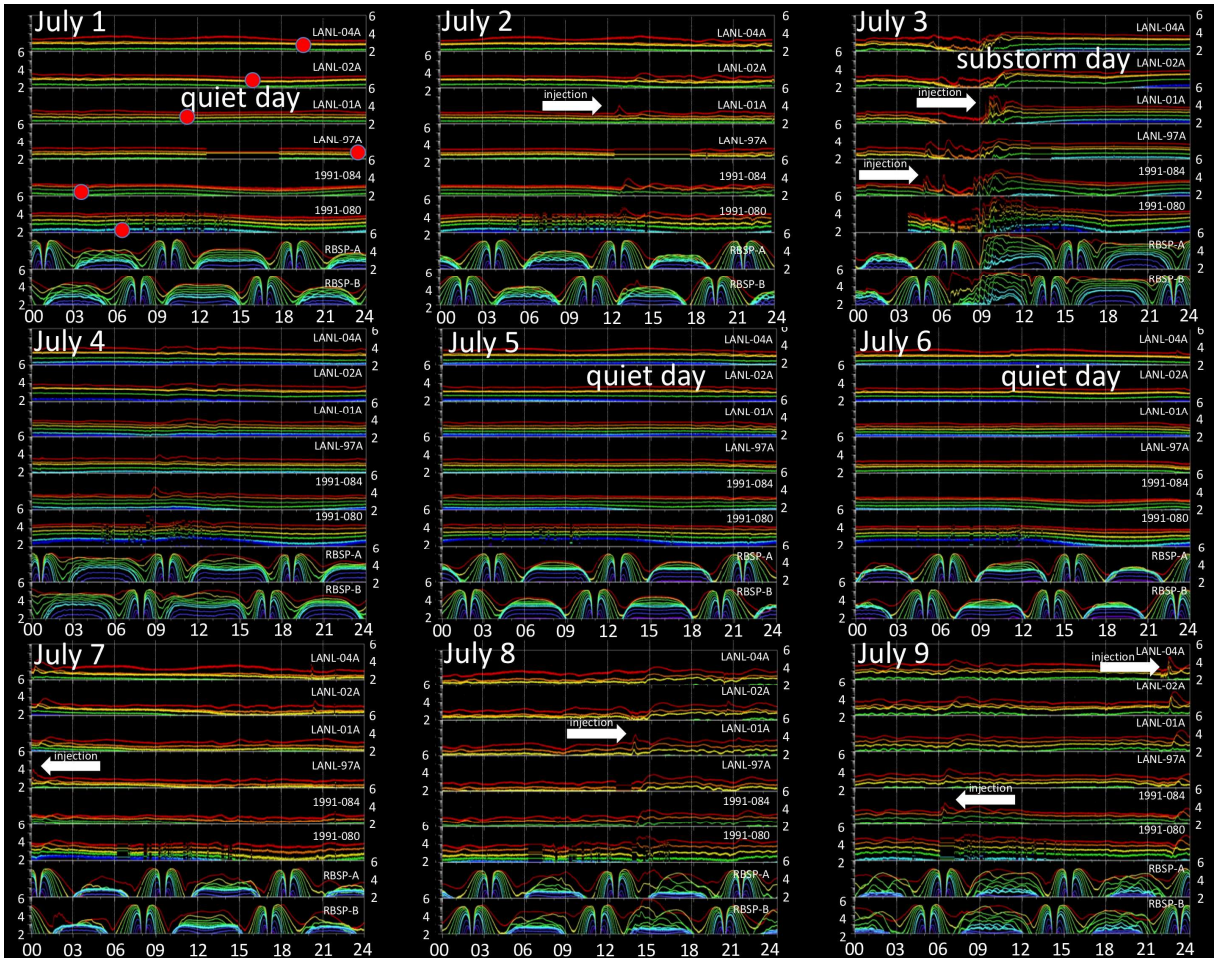

Figure 2: LANL-GEO (from top to bottom: LANL-04A, LANL-02A, LANL-01A, LANL-97A, 1994-084, 1991-080) and Van Allen Probes (RBSP B and RBSP A) survey electron flux from 1 to 10 July 2014 with one panel per day. This figure shows rather quiet days (on July 1, 5, 6) and mild (on July 2, 4, 7) to moderate (on July 3, 8, 9) perturbations from substorm activity. White arrows point to some of the main injections. (red circle) Local MLT midnight for each LANL-GEO satellite changes by less than five minutes during the 10-day period (1991-080: 6.33, 1991-084: 3.33, LANL-97A: 23.38, LANL-01A: 11.29, LANL-02A: 15.43, LANL-04A: 19.53).

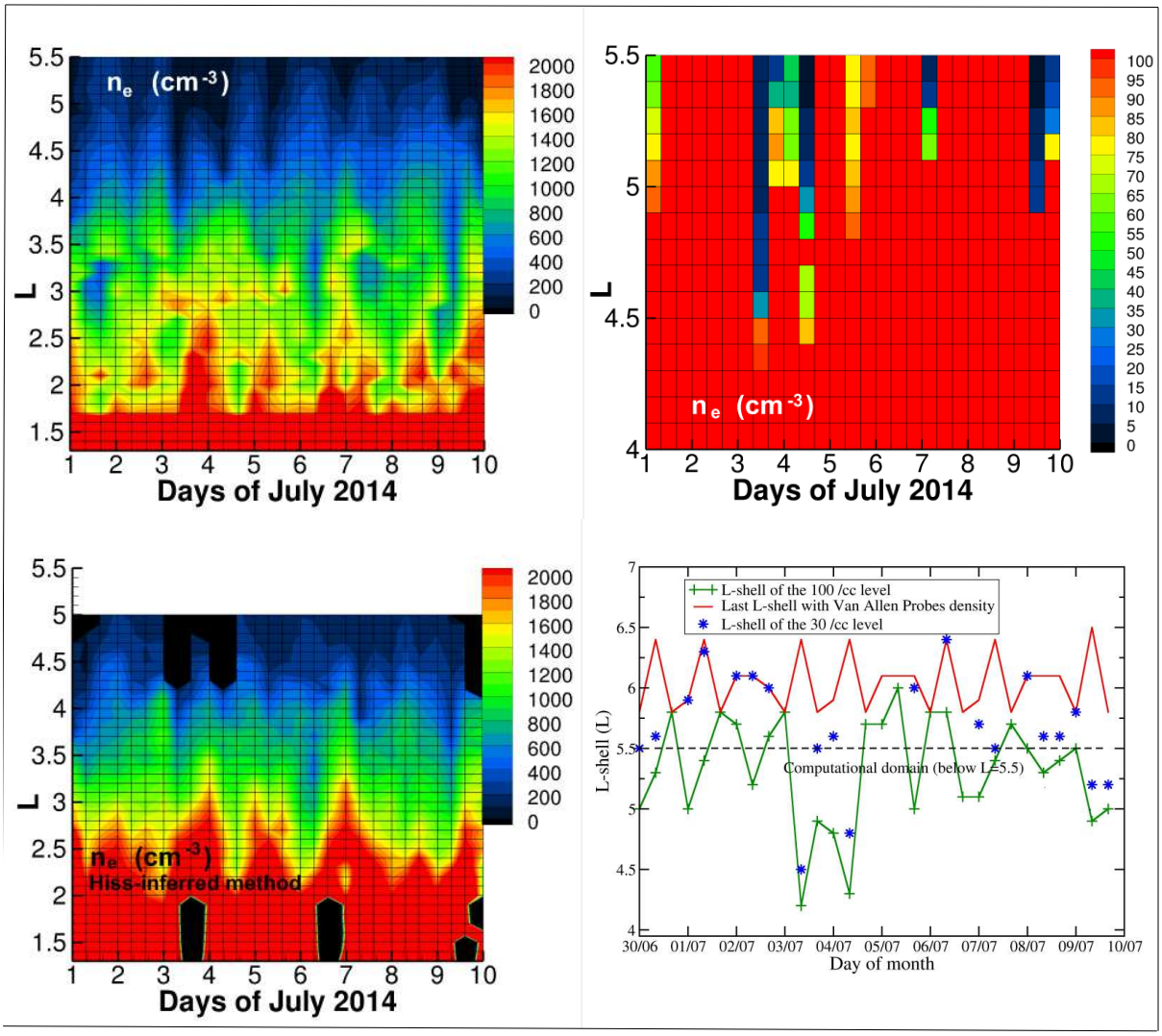

Figure 3: Evolution of the plasma density during the first 10 days of July 2014. (top left) plasma density from EMFISIS. (top right) Zoom above L=4 for density below 100 #/cc in order to define the plasmapause region. (bottom left) Estimation of the plasma density up to L=5 from the whistler-mode hiss waves used as a verification of the density and the hiss presence. (bottom right) L-shell of the last Van Allen Probes known density, 100 /cc density level, and 30/cc density level showing all plasmas densities used in the domain of this study come from Van Allen Probes measurement. The region of density between 30/cc and 100 /cc, defined here as the *dense* plasmapause region, is a widely

spread region over L-shell, except during short times of injections and compressed plasmasphere.

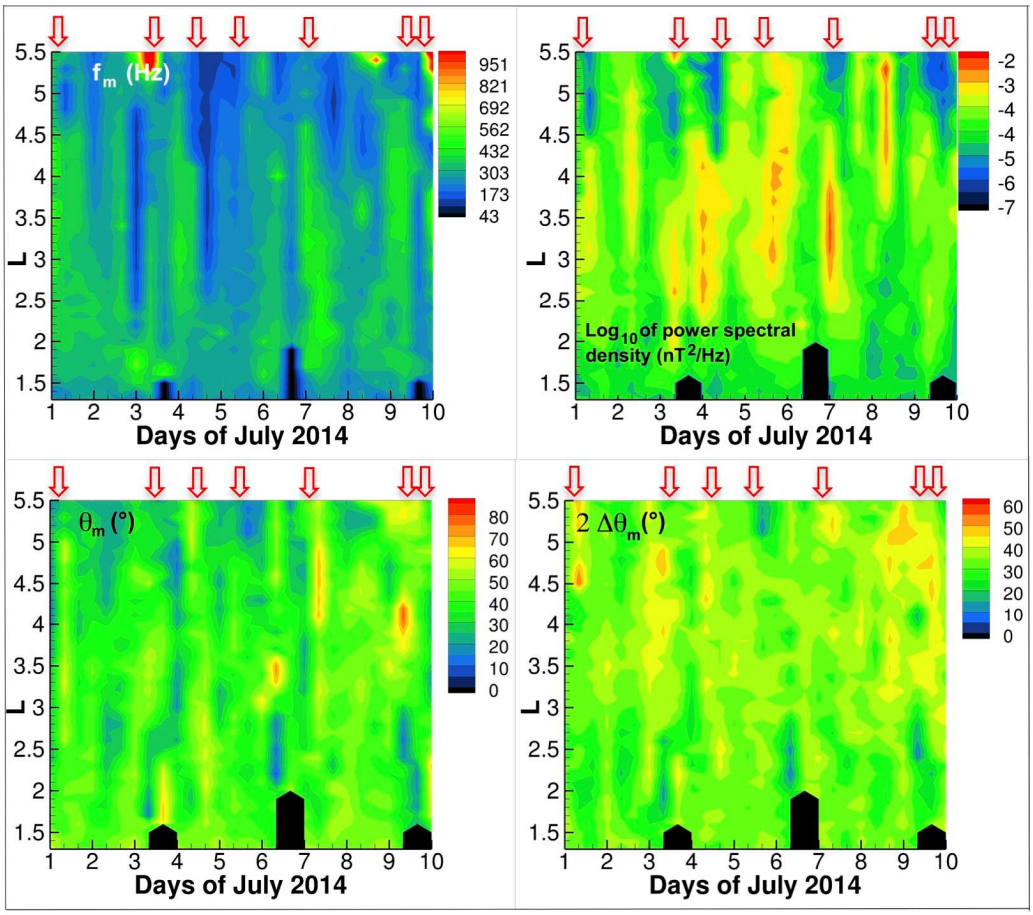

Figure 4: Evolution of the whistler-mode wave properties during the first 10 days of July 2014; (top left) mean frequency, (top right) wave power spectral density, (bottom left) mean wave normal angle and (bottom right) wave normal angle width. Most of the whistler-mode waves here are plasmaspheric hiss. Exceptions occur, for instance, on July 3 and 10. The times at which the plasma density (cf. Figure 3) is perturbed by substorm injections (cf. Figure 2) are identified by red arrows.

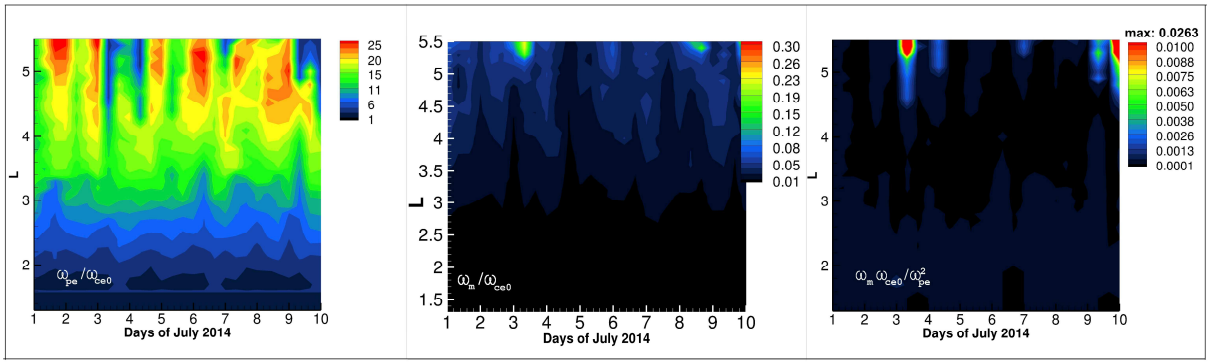

Figure 5: (left) The ratio of the plasma frequency to the equatorial gyrofrequency (f_{pe}/f_{ce0}) for the first 10 days of July 2014. Verification of the (middle) low frequency ($\omega_m/\omega_{ce0} < 1$) and (right) dense plasma ($\omega_m\omega_{ce0}/\omega_{pe}^2 \ll 1$) limits taken in the computation of the diffusion coefficients. To be valid, the first limit (Figure 4, middle) has to be lower than ~0.1 and the second (Figure 4, right) lower than ~0.01. This corresponds to black and blue regions (i.e. almost everywhere), thus giving confidence in the results for most of the domain. Small exceptions are noticeable on the July 3 and 10 above L=5.2, in concordance with the main substorm (July 3) and the high-speed solar wind-stream (July 10). During the various substorms on July 3, 4, 7 and the HSS, f_{pe}/f_{ce0} drops by a factor ~4, from 20-25 down to ~6.

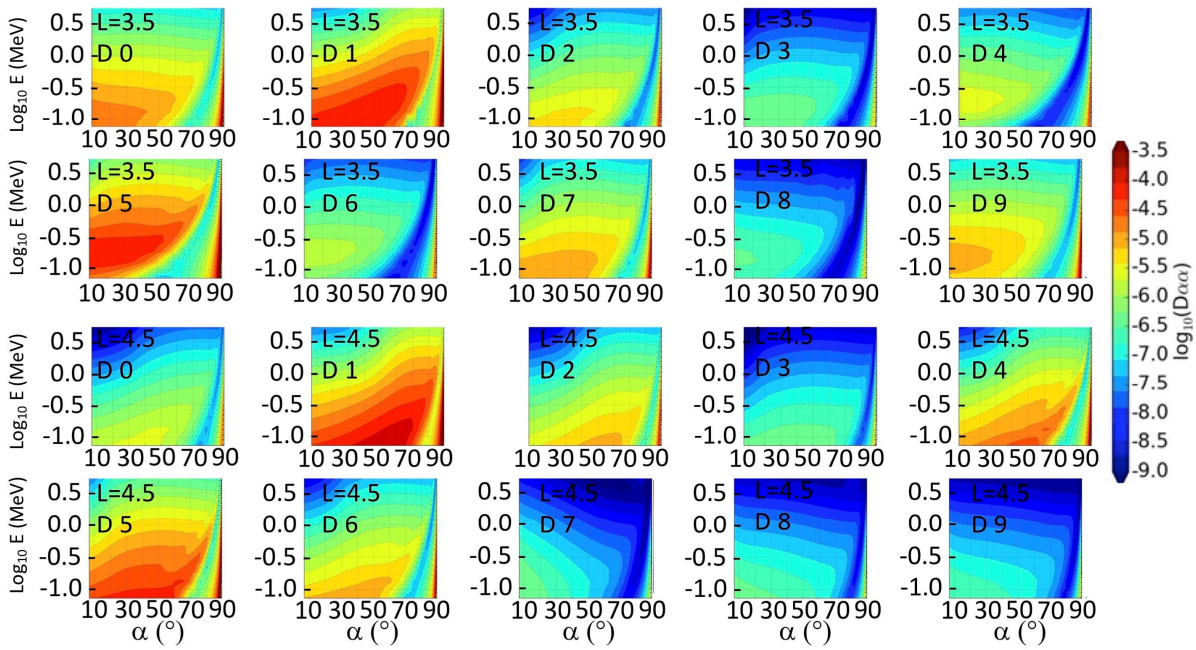

Figure 6: Diffusion coefficients in the (Energy, pitch angle) plane, shown for the first 8 hour interval of each day of the 10-day period at (top two rows) L=3.5 and (bottom two rows) L=4.5. This shows the daily variability of the diffusion coefficients at fixed L-shell.

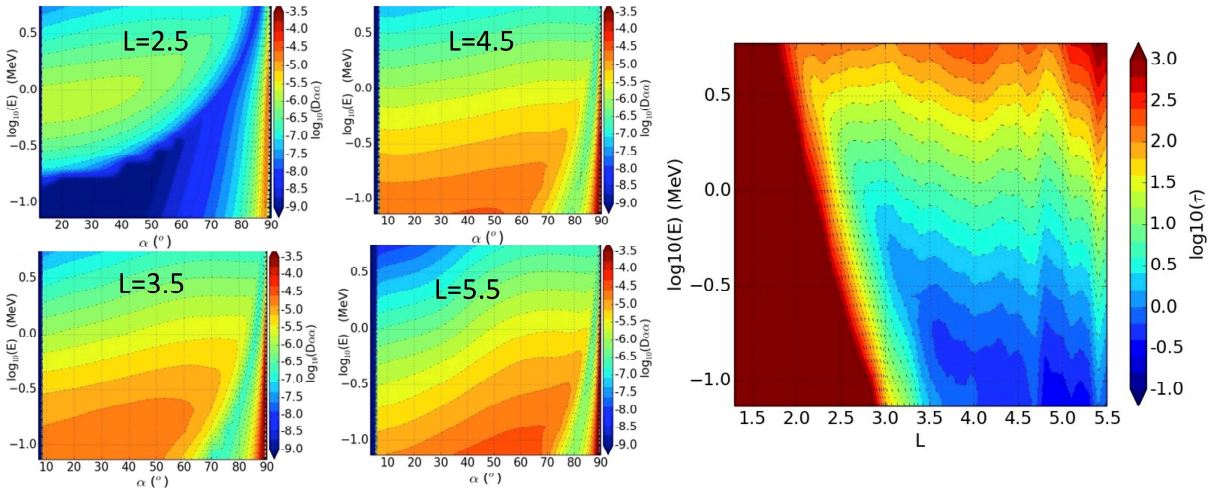

Figure 7: (left) Averaged diffusion coefficients log10($D_{\alpha\alpha}$) (log10 of s^{-1}) for the period of interest, plotted at fixed L = 2.5, 3.5, 4.5, 5.5 in the (E, α) plane. At fixed L shell, maximal cyclotron pitch angle diffusion occurs at higher energy as pitch angle increases (for α ≤ 70°). (right) Averaged electron lifetime in the (L, E) plane for the period of interest, showing 2 regions of high scattering above and below L~4.7 for of electrons of less than ~500 keV, which are discussed in section 3.3.

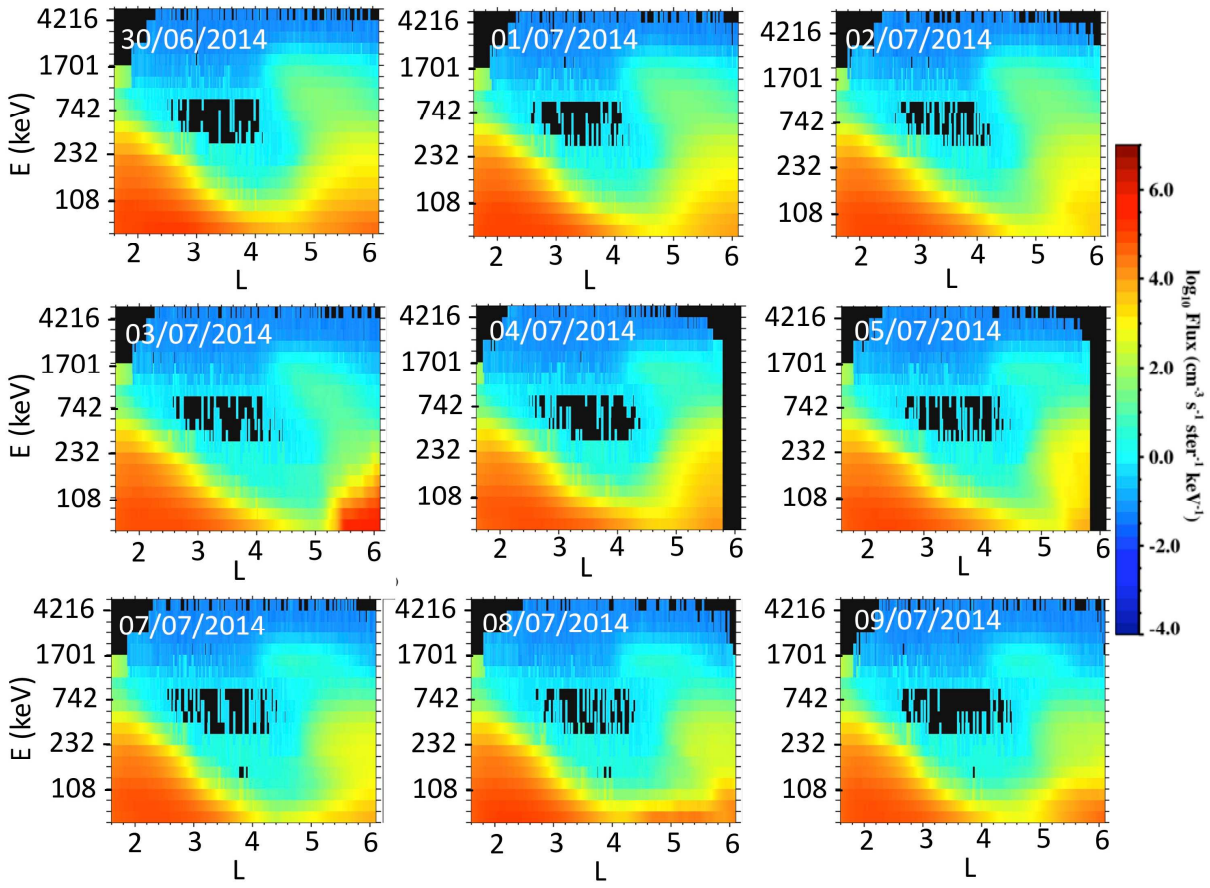

Figure 8: Snapshots of MagEis measurements in the (L shell, Energy) plane of the electron flux for each outbound path (~8h), unless unavailable, from June 30 to July 9 2014 (omitting July 6). We observe the slot region forming between the belts during 10 days and gradual removal of the outer belts. Substorm activity is also visible, e.g., on the July 3, with influx of electrons below ~200 keV.

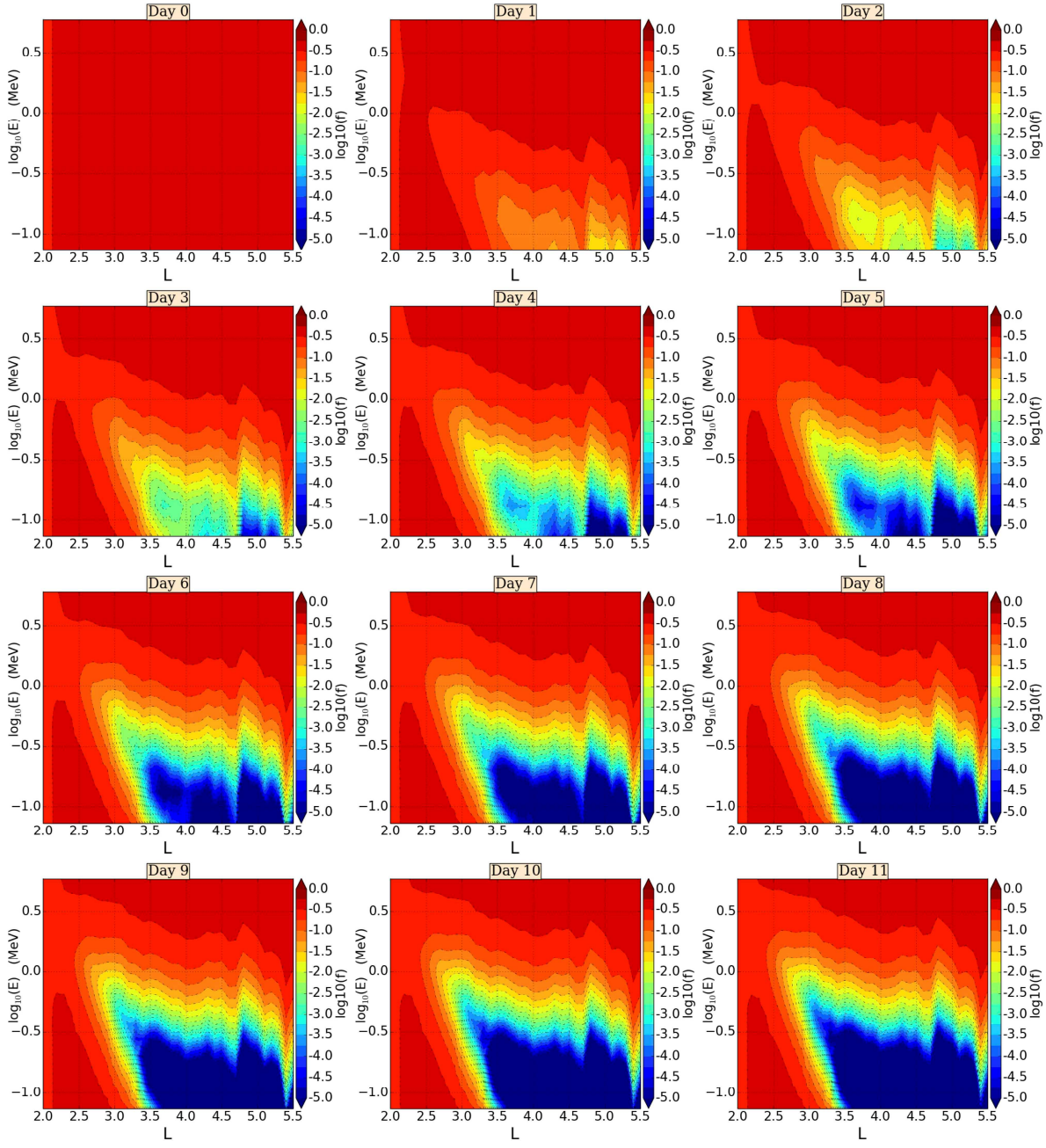

Figure 9: Evolution of the simulated omnidirectional flux during 12 days, plotted at the beginning of each day. The first panel (Day 0) indicates the initial condition that is homogeneous in energy.

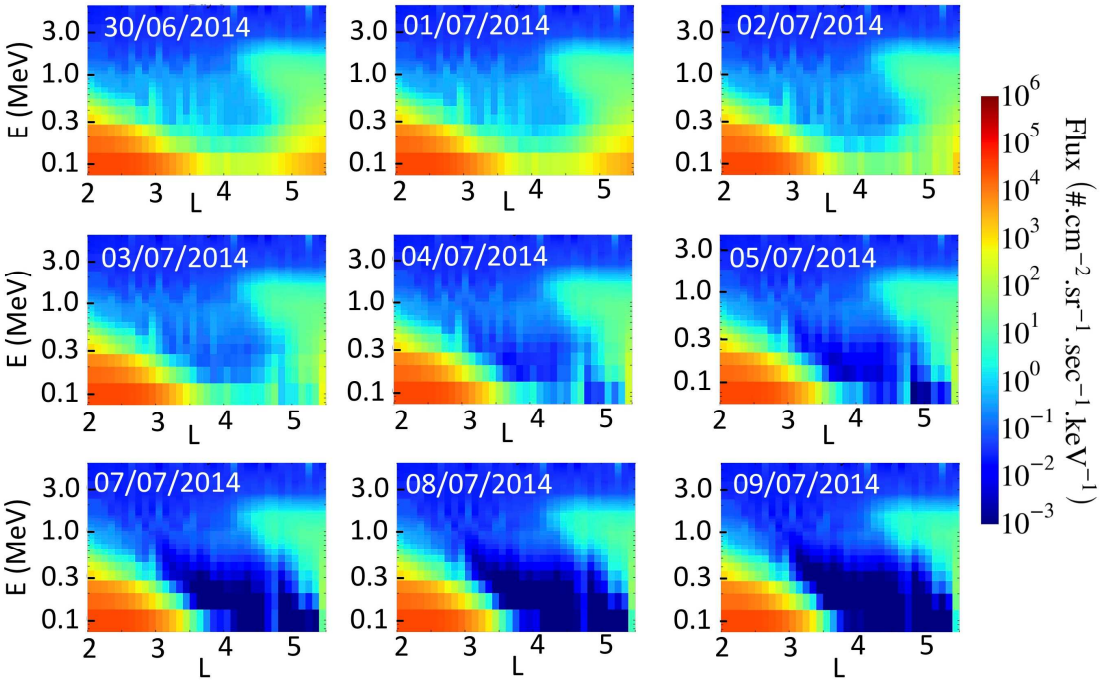

Figure 10: Evolution of the simulated omnidirectional flux from 06/30/2014 to 07/10/2014, plotted at the beginning of each day (omitting the 06/10/2014). The first panel (Day 0) indicates the initial condition given by the MagEIS spin-averaged flux on 30/06/2014 6:54-11:31 (first panel of Figure 7).